The 8th European Congress on Computational Methods in Applied Sciences and Engineering
ECCOMAS Congress 2022
5-9 June 2022, Oslo, Norway

A THERMO-COUPLED CONSTITUTIVE MODEL FOR SEMI-CRYSTALLINE POLYMERS AT FINITE STRAINS: APPLICATION TO VARYING DEGREES OF CRYSTALLINITY AND TEMPERATURES

M. Reuvers[1,*], B. Boes[1], S. Felder[1], T. Brepols[1] and S. Reese[1]

[1] Institute of Applied Mechanics, RWTH Aachen University, Mies-van-der-Rohe-Str. 1, D-52074 Aachen, Germany
{marie.reuvers, birte.boes, sebastian.felder, tim.brepols, stefanie.reese}
@ifam.rwth-aachen.de

Key words: Semi-crystalline polymers, Finite strains, Thermo-mechanical coupling, Viscoplasticity

Abstract. Thermoplastic materials are widely used for thermoforming and injection moulding processes, since their low density in combination with a high strength to mass ratio are interesting for various industrial applications. Semi-crystalline polymers make up a subcategory of thermoplastics, which partly crystallize after cool-down from the molten state. During the thermoforming process, residual stresses can arise, due to complex material behavior under different temperatures and strain rates. Therefore, computational models are needed to predict the material response and minimize production errors. This work presents a thermo-mechanically consistent phenomenological material formulation at finite strains, based on [1]. In order to account for the highly nonlinear material behavior, elasto-plastic and visco-elastic contributions are combined in the model formulation. To account for the crystalline regions, a hyperelastic-plastic framework is chosen, based on [2, 3]. Kinematic hardening of Arruda-Boyce form is incorporated in the formulation, as well as associated plastic flow. The material parameters depend on both, the temperature as well as the degree of crystallinity. A comparison to experiments with varying degrees of crystallinity and temperatures is presented, where a special blending technique ensures stable crystallinity conditions.

1 INTRODUCTION

Semi-crystalline polymers (SCP) are used in many different industry applications due to their high strength to weight ratio, their temperature stability and their potential for cost-effective mass production. Hereby, their manufacturing process plays a crucial role for the latter material behavior, since several factors like thermal treatment, applied stresses, moisture level and even the manufacturing process itself have a huge influence on the resulting material [4]. This complex material behavior stems from the underlying biphasic microstructure of SCPs, where ductile amorphous regions are combined with hard crystalline ones which impedes reliable material predictions. Consequently, a wide range of material models have been established during the last decade, aiming to account for that problem. Here, earlier works regarding a phenomenological approach by [5] and [6] introduced an additive decomposition of the resistance

into an intermolecular and molecular network. These works laid the foundation for various models in the field of amorphous (see [2, 7]) and semi-crystalline (see [8, 9, 10]) polymers, to name a few.
In this work ,a coupled visco-elastic, visco-plastic model approach is proposed (see Section 2), following the works of e.g. [11, 12, 13, 14], to accurately predict the observed plastic behavior, as well as strain recovery, stress relaxation and loading-unloading hysteresis loop. In addition, the presented model formulation accounts for the influence of temperature which has been studied by e.g. [15, 16], in terms of a full thermomechanical coupling. The influence of the degree of crystallinity (DOC) on the material behavior is taken into account. Here, the DOC serves as a constant input parameter, as done in [17]. To improve the results of [17], tension-compression asymmetry in yielding is incorporated, as done by [18, 19]. The novelty of the proposed framework, is the dependence of the material parameters on the DOC as well as temperature. In this way the yield surface is able to evolve its shape throughout the evolution of temperature and adapt to the changing model behavior. The model is then implemented as a material user subroutine UMAT into the ABAQUS framework and characterized using experimental results (see Section 3). In Section 3, the capabilities of the proposed formulation are shown, first by a model prediction at a higher strain rate and then in a multiaxial stress state for a structural validation example. Finally, in Section 4 a conclusion is drawn.

2 MATERIAL MODEL FORMULATION

The objective of this work is the derivation of a thermomechanically coupled constitutive framework to predict the material behavior of semi-crystalline polymers under thermomechanical loading conditions in tension and compression. In addition to the displacement and temperature field, the degree of crystallinity is introduced as a constant input parameter which influences the material properties, as can be seen in Table 3.1. In this manner, the biphasic nature of the underlying microstructure is treated in a continuum mechanical way, where the total degree of crystallinity is considered as a scalar quantity, instead of making a differentiation between the two underlying crystal configurations (γ-phase and α-phase). In Figure 1, a schematic illustration on the basis of a rheological model of the proposed thermomechanically coupled framework and Helmholtz free energy is presented. With the assumption of two decoupled processes, a decomposition into an elasto-plastic (index 1) and a visco-elastic (index 2) model contribution is chosen, following the works of e.g. [1, 2]. A defect energy of Arruda-Boyce type, represented as a nonlinear spring, is incorporated in the plastic model branch to account for kinematic hardening. With this approach, the elastic, visco-hyperelastic, and visco-hyperelastic-plastic material response, observed in experiments of e.g. [1], can be depicted.

2.1 Kinematics

The kinematic relations needed to extend the presented rheological model (cf. Figure 1) in a continuum mechanical way to finite strains, are based on several multiplicative decompositions of the total deformation gradient $\boldsymbol{F}$. In the elasto-plastic part, the deformation gradient, $\boldsymbol{F} = \boldsymbol{F}_{e1}\,\boldsymbol{F}_p$, is decomposed into an elastic $\boldsymbol{F}_{e1}$ and plastic $\boldsymbol{F}_p$ part (cf. [20, 21, 22]) with the concomitant introduction of a plastic intermediate configuration ic_1 . For the viscous part, a

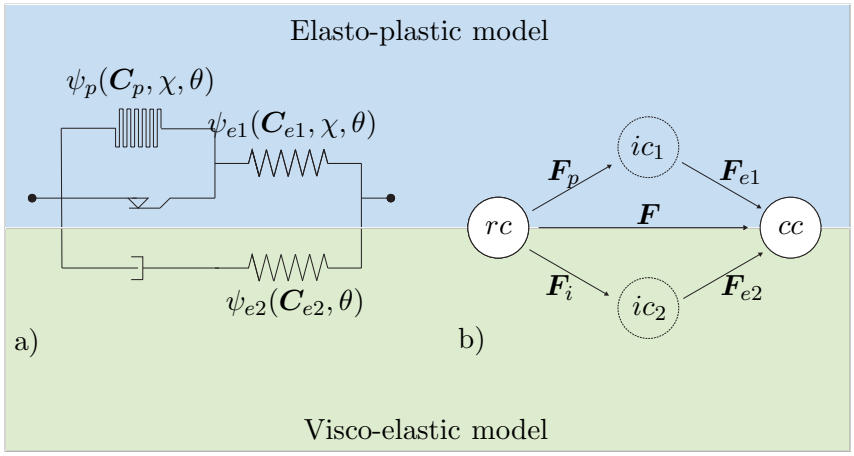

Figure 1: a) Schematic illustration of the constitutive model b) Multiplicative splits of the deformation gradient

split into elastic and inelastic parts, $\boldsymbol{F} = \boldsymbol{F}_{e2}\,\boldsymbol{F}_i$, is performed, respectively. In this way, an additional inelastic intermediate configuraton ic_2 is introduced, in line with the works of e.g. [23, 24, 25].

2.2 Helmholtz free energy

In line with the aforementioned assumptions (cf. Fig. 1), the total Helmholtz free energy is introduced as the sum of the elasto-plastic ψ_1 as well as the visco-elastic ψ_2 contribution and an additional energy term ψ_c which represents a caloric contribution related to the temperature-dependent specific heat of the material

$$\psi = \psi_1 + \psi_2 + \psi_c. \tag{1}$$

Here, the free energy associated with elastoplasticity

$$\psi_1 = \psi_{e1}(\mathbf{C}_{e1}, \chi, \theta) + \psi_p(\boldsymbol{C}_p, \chi, \theta) \tag{2}$$

consists of an elastic term ψ_{e1} as well as the defect energy ψ_p associated with plastic deformations, whereas the viscous Helmholtz free energy consists of an elastic energy ψ_{e2} only

$$\psi_2 = \psi_{e2}(\mathbf{C}_{e2}, \theta). \tag{3}$$

The total Helmholtz free energy depends on the elastic right Cauchy-Green tensors as well as the plastic right Cauchy-Green tensor

$$\boldsymbol{C}_{e1} = \boldsymbol{F}_{e1}^T\,\boldsymbol{F}_{e1} = \boldsymbol{F}_p^{-T}\,\boldsymbol{C}\,\boldsymbol{F}_p^{-1}, \qquad \boldsymbol{C}_{e2} = \boldsymbol{F}_{e2}^T\,\boldsymbol{F}_{e2} = \boldsymbol{F}_i^{-T}\,\boldsymbol{C}\,\boldsymbol{F}_i^{-1}, \qquad \boldsymbol{C}_p = \boldsymbol{F}_p^T\,\boldsymbol{F}_p, \tag{4}$$

respectively. Here, $\boldsymbol{C} = \boldsymbol{F}^T\boldsymbol{F}$ represents the right Cauchy-Green tensor. All energetic contributions are functions of temperature θ and/or degree of crystallinity χ to incorporate thermal influences as well as the morphology of the underlying material microstructure. Thereby, an increasing temperature leads to a decrease of all energetic contributions, whereas a higher degree of crystallinity results in a stiffer material response in the elasto-plastic part. The specific choices for all free energies are discussed in Section 2.6.

2.3 Derivation based on the Clausius-Duhem inequality

The derivation of the constitutive relations is based on the local form of the Clausius-Duhem inequality

$$\boldsymbol{S} : \frac{1}{2}\dot{\boldsymbol{C}} - \rho_0(\dot{\psi} + \eta\dot{\theta}) - \frac{1}{\theta}\,\boldsymbol{q}_0 \cdot \mathrm{Grad}(\theta) \geq 0 \tag{5}$$

to ensure the fullfillment of the second law of thermodynamics. In the inequality, the specific entropy is defined as η and the density and heat flux with respect to the reference configuration are stated as ρ_0 and $\boldsymbol{q}_0$, respectively. Inserting the specific Helmholtz free energy (1) and utilizing the chain rule of differentiation yields

$$\begin{aligned}\boldsymbol{S} : \frac{1}{2}\dot{\boldsymbol{C}} - \rho_0\bigg(\frac{\partial\psi}{\partial\boldsymbol{C}_{e1}} : \dot{\boldsymbol{C}}_{e1} + \frac{\partial\psi}{\partial\boldsymbol{C}_{p}} : \dot{\boldsymbol{C}}_{p} + \frac{\partial\psi}{\partial\boldsymbol{C}_{e2}} : \dot{\boldsymbol{C}}_{e2}\bigg) \\ -\rho_0\bigg(\frac{\partial\psi}{\partial\theta} + \eta\bigg)\dot{\theta} - \frac{1}{\theta}\boldsymbol{q}_0 \cdot \mathrm{Grad}(\theta) \geq 0.\end{aligned} \tag{6}$$

Afterwards, the expression is further reformulated, exploiting the plastic velocity gradient $\boldsymbol{L}_p = \dot{\boldsymbol{F}}_p\boldsymbol{F}_p^{-1}$ under the assumption that ψ_{e1}, ψ_{e2} and ψ_p are isotropic functions of $\boldsymbol{C}_{e1}, \boldsymbol{C}_{e1}$ and $\boldsymbol{C}_p$, respectively. Note here, that the degree of crystallinity χ serves as a constant input parameter in this formulation. The complete derivation is omitted here, but can be found, for example, in [26]. After reformulation, several stress quantities are introduced in line with [1, 3, 25]. Corresponding to the elastoplastic model contribution, the second Piola-Kirchhoff stress tensor $\boldsymbol{S}_1$ and the Mandel stress tensor $\boldsymbol{M}_1$

$$\boldsymbol{S}_1 = 2\rho_0\boldsymbol{F}_p^{-1}\frac{\partial\psi_{e1}}{\partial\boldsymbol{C}_{e1}}\boldsymbol{F}_p^{-T}, \quad \boldsymbol{M}_1 = 2\rho_0\boldsymbol{C}_{e1}\frac{\partial\psi_{e1}}{\partial\boldsymbol{C}_{e1}} \tag{7}$$

are introduced with respect to the reference and plastic intermediate configuration, respectively. In addition, the back stress $\boldsymbol{X}$ in the intermediate plastic configuration, related to kinematic hardening, is given as

$$\boldsymbol{X} = 2\rho_0\boldsymbol{F}_p\frac{\partial\psi_p}{\partial\boldsymbol{C}_p}\boldsymbol{F}_p^{T}. \tag{8}$$

Similarly, for the visco-elastic part

$$\boldsymbol{S}_2 = 2\rho_0\boldsymbol{F}_i^{-1}\frac{\partial\psi_{e2}}{\partial\boldsymbol{C}_{e2}}\boldsymbol{F}_i^{-T}, \quad \boldsymbol{M}_2 = 2\rho_0\boldsymbol{C}_{e2}\frac{\partial\psi_{e2}}{\partial\boldsymbol{C}_{e2}} \tag{9}$$

are the second Piola-Kirchhoff and Mandel stress tensor corresponding to the reference and inelastic intermediate configuration, respectively. Inserting the above derived stress measures back into the Clausius-Duhem inequality leads to:

$$\frac{1}{2}\left(\boldsymbol{S} - \boldsymbol{S}_1 - \boldsymbol{S}_2\right) : \dot{\boldsymbol{C}} + \left(\boldsymbol{M}_1 - \boldsymbol{X}\right) : \boldsymbol{D}_p + \boldsymbol{M}_2 : \boldsymbol{D}_i - \rho_0\left(\frac{\partial\psi}{\partial\theta} + \eta\right)\dot{\theta} - \frac{1}{\theta}\boldsymbol{q}_0 \cdot \mathrm{Grad}(\theta) \geq 0, \tag{10}$$

where $\boldsymbol{D}_{(*)} = \mathrm{sym}\left(\boldsymbol{L}_{(*)}\right)$ denotes the symmetric part of the corresponding velocity gradient $\boldsymbol{L}_{(*)} = \dot{\boldsymbol{F}}_{(*)}\,\boldsymbol{F}_{(*)}^{-1}$, with $(*) = i, p$. Using the relation $\boldsymbol{S} = \boldsymbol{S}_1 + \boldsymbol{S}_2$ for the second Piola-Kirchhoff stress as well as $\eta = -\partial\psi/\partial\theta$ for the entropy leads to the reduced form of (10)

$$(\boldsymbol{M}_1 - \boldsymbol{X}) : \boldsymbol{D}_p + \boldsymbol{M}_2 : \boldsymbol{D}_i \geq 0. \tag{11}$$

Here, Fourier's law was used to define the heat flux

$$\boldsymbol{q}_0 \quad = -J\, \lambda_T\, \boldsymbol{C}^{-1}\, \mathrm{Grad}(\theta) \tag{12}$$

with $J = \det\boldsymbol{F}$ and $\lambda_T(\theta)$ denoting the heat conductivity, to ensure positivity of the dissipation inequality during conduction.

2.4 Evolution equations

2.4.1 Yield criterion and plastic evolution equations

Following [19], a parabolic Tschoegel-type (c.f. [28]) yield function is considered

$$\Phi_p = 3J_2 + (m-1)\sigma_t I_1 - m\,\sigma_t^2 \leq 0 \tag{13}$$

which is influenced by kinematic hardening via the stress $\boldsymbol{\Sigma} = \boldsymbol{M}_1 - \boldsymbol{X}$ that enters the function in terms of the first $I_1 = \mathrm{tr}(\boldsymbol{\Sigma})$ and second deviatoric invariant $J_2 = 1/2\,\mathrm{tr}(\mathrm{dev}(\boldsymbol{\Sigma})^2)$. The use of the additional invariant I_1 ensures correct yielding behavior under hydrostatic pressure as shown by [27] for nylon 101, compared to e.g. a classical von Mises-type yield surface. Here, the ratio m is a measure for the tension-compression flow asymmetry

$$m = \frac{\sigma_c(\chi,\theta)}{\sigma_t(\chi,\theta)}, \tag{14}$$

where σ_c and σ_t are the compressive and tensile yield strengths, respectively. Both material parameters depend on temperature and degree of crystallinity. Using the yield surface, the plastic flow rule in the plastic intermediate configuration ic_1 follows as

$$\boldsymbol{D}_p = \dot{\lambda}_p \frac{\partial \Phi_p}{\partial \boldsymbol{M}_1} = \dot{\lambda}_p \Big(3\mathrm{dev}(\boldsymbol{\Sigma}) + (m-1)\,\sigma_t\, \boldsymbol{I} \Big) \tag{15}$$

with $\dot{\lambda}_p$ being the plastic multiplier. Finally, the Karush-Kuhn-Tucker conditions are given as

$$\dot{\lambda}_p \geq 0, \quad \Phi_p \leq 0, \quad \dot{\lambda}_p\, \Phi_p = 0. \tag{16}$$

2.4.2 Viscous model

The evolution of the viscous deformation in the inelastic intermediate configuration ic_2 is chosen as

$$\boldsymbol{D}_i = \frac{1}{2\tau\mu_2}\mathrm{dev}(\boldsymbol{M}_2) + \frac{1}{9\tau K_2}\mathrm{tr}(\boldsymbol{M}_2)\boldsymbol{I} \tag{17}$$

according to the work of [25], with the bulk modulus $K_2(\theta)$ and shear modulus $\mu_2(\theta)$. For the relaxation time τ a constant is assumed, since experimental data for the characterization has not been available yet.

2.5 Representation in the reference configuration

As shown in the previous sections, the constitutive equations of the model are defined in various configurations. To reduce the number of internal variables needed, a pull-back operation (see [26] for a detailed overview) to the reference configuration is performed. In this way, the model depends only on a few symmetric internal variables. Moreover, this procedure allows for the application of an efficient and robust exponential map algorithm to integrate the plastic evolution equations which preserves the symmetry of the internal variables, as well as the plastic incompressibility as shown in [3].

2.6 Specific choice for the Helmholtz free energy

So far, the constitutive framework was introduced in a general manner without specifying the Helmholtz free energies for the elasto-plastic and visco-elastic parts in order to maintain a flexible derivation. In this way, the presented model formulation can be adapted easily for other materials.

2.6.1 Free energy of the elasto-plastic part

For the elastic energy of the elasto-plastic part a compressible Neo-Hookean-type function is chosen

$$\psi_{e1} = \frac{\mu_1}{2}\left(\mathrm{tr}(\mathbf{C}_{e1}) - 3\right) - \mu_1 \ln\left(J_{e1}\right) + \frac{\Lambda_1}{4}\left(\det(\mathbf{C}_{e1}) - 1 - 2\ln(J_{e1})\right) - 3\,K_1\alpha_T(\theta-\theta_0)\ln(J_{e1}), \tag{18}$$

depending on the two Lamé constants $\mu_1(\theta,\chi)$ and $\Lambda_1(\theta,\chi)$ and the thermal expansion coefficient $\alpha(\theta)$. Kinematic hardening is introduced by the use of an Arruda-Boyce (see [29]) type defect energy

$$\psi_p = \mu^* \sum_{i=1}^{5} \frac{c_i}{\lambda_m^{2i-1}(I_{1p}^i - 3^i)}. \tag{19}$$

Here, $I_{1p} = \mathrm{tr}(\boldsymbol{C}_p)$ is the first invariant of the plastic right Cauchy Green tensor. ψ_p depends on the two material parameters λ_m and μ^* [30]. The prefactor c_i is defined as

$$c_i = \left\{\frac{1}{2},\quad \frac{1}{20},\quad \frac{11}{1050},\quad \frac{19}{7000},\quad \frac{519}{673760}\right\}. \tag{20}$$

With Eq. (18) and (19), the second Piola Kirchhoff stress for the elastoplastic part and the thermodynamic conjugate force for kinematic hardening in the reference configuration follow to

$$\boldsymbol{S}_1 = \mu_1(\boldsymbol{C}_p^{-1} - \boldsymbol{C}^{-1}) + \frac{\Lambda_1}{2}\left(\frac{\det(\boldsymbol{C})}{\det(\boldsymbol{C}_p)} - 1\right)\boldsymbol{C}^{-1} - 3K_1\alpha_T(\theta-\theta_0)\boldsymbol{C}^{-1} \tag{21}$$

$$\bar{\boldsymbol{X}} = \mu^*\left(\boldsymbol{I} + \frac{1}{5\lambda_m} I_{1p}\boldsymbol{I} + \frac{11}{175\lambda_m^2} I_{1p}^2\boldsymbol{I} + \frac{19}{875\lambda_m^3} I_{1p}^3\boldsymbol{I} + \frac{519}{67375\lambda_m^4} I_{1p}^4\boldsymbol{I}\right) \tag{22}$$

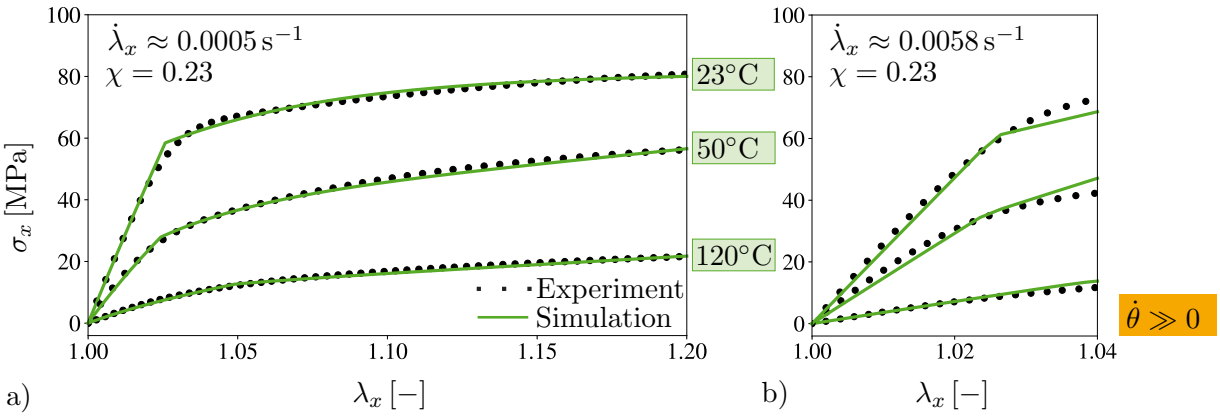

Figure 2: Monotonic, uniaxial extension: Comparison of experimental data and corresponding model response for 23% crystallinity a) Model characterization at $\dot{\lambda}_x = 0.0005\,s^{-1}$ loading rate b) Model prediction at $\dot{\lambda}_x = 0.0058\,s^{-1}$ loading rate.

2.6.2 Free energy of the viscous part

The Helmholtz free energy corresponding to the viscous part is chosen as of Neo-Hookean type

$$\psi_2 = \frac{\mu_2}{2}\left(\mathrm{tr}(\mathbf{C}_{e2}) - 3\right) - \mu_2 \ln(J_{e2}) + \frac{\Lambda_2}{4}\left(\det(\mathbf{C}_{e2}) - 1 - 2\ln(J_{e2})\right) - 3\,K_2\alpha_T(\theta-\theta_0)\ln(J_{e2}), \tag{23}$$

as a function of the Lamé constants $\mu_2(\theta)$ and $\Lambda_2(\theta)$. After a longer derivation, the second Piola Kirchhoff stress for the viscous part results in

$$\boldsymbol{S}_2 = \mu_2(\boldsymbol{C}_i^{-1} - \boldsymbol{C}^{-1}) + \frac{\Lambda_2}{2}\left(\frac{\det(\boldsymbol{C})}{\det(\boldsymbol{C}_i)} - 1\right)\boldsymbol{C}^{-1} - 3K_2\alpha_T(\theta-\theta_0)\boldsymbol{C}^{-1} \tag{24}$$

2.7 Numerical implementation

The material model is embedded into the commercial FEM software ABAQUS/Standard as a user subroutine UMAT. For details regarding the implementation as as well as the algorithmic treatment of the constitutive equations corresponding to the elasto-plastic model, the reader is reffered to [1, 3, 17].

3 NUMERICAL EXAMPLES

3.1 Model characterization

In the following section, the isothermal material model is characterized using experimental monotonic tensile data from [17] for different temperatures, a constant degree of crystallinity $\chi = 0.23$ and a constant stretch rate $\dot{\lambda}_x \approx 0.0005 s^{-1}$. Therefore a staggered parameter identification procedure is exploited, where the Young's modulus is taken from the initial elastic response of the material during monotonic loading. The elastic model parameters are defined as follows

$$E_{Exp}(\theta, \chi) = E_1(\theta, \chi) + E_2(\theta). \tag{25}$$

Note here, that for simplicity only the elasto-plastic Young's modulus E_1 depends on the degree of crystallinity. In addition, the initial yield stress $\sigma_t = \chi\sigma_{t,0}(\theta)$ in tension is taken from the experimental results of [17]. The missing plastic parameters can be identified using a nonlinear multiple curve fitting procedure in MATLAB, employing the Downhill-Simplex algorithm. Note here, that the thermal, as well as the viscous parameters are taken from [17]. Resulting from the staggered identification scheme, a set of mechanical parameters is defined for each temperature separately (see Table 3.1). In Table 3.1, also the accompanying thermal parameters are stated. The corresponding material response to monotonic tensile results at different temperatures can be seen in Fig. 2. To test the characterized material model, a higher strain rate of $\dot{\lambda}_x \approx 0.0058s^{-1}$ is used for a model prediction (see Fig. 2). Note here, that the results above four percent strain are left out (see Fig. 2), due to a prominent self-heating effect, visible in the experimental data. The prediction reveals good agreement with the experimental data, especially for temperatures above the glass transition temperature. As alluded in [1, 17], material self-heating occured at higher loading rates. Consequently, the model prediction is only shown up until $\lambda_x = 1.04$.

Table 1: a) Temperature dependent mechanical parameters b) Thermal material parameters

a)

Function	Parameter at:	23 °C	50 °C	120 °C
$E_1 = \chi E_{1,0}(\theta)$	$E_{1,0}$ [MPa]	7392.6	3016.9	798.26
$E_2 = E_2(\theta)$	E_2 [MPa]	677	639.23	183.6
$\nu_1 = \nu_2$	ν_1 [-]	0.35	0.35	0.35
$\sigma_t = \chi\sigma_{t,0}(\theta)$	$\sigma_{t,0}$ [MPa]	71	49	30
$\sigma_c = \chi\sigma_{c,0}(\theta)$	$\sigma_{c,0}$ [MPa]	284	53.9	30
$\mu^* = \chi\mu_0^*(\theta)$	μ_0^* [MPa]	75	110	120
$\lambda = \lambda(\theta)$	λ [-]	4	1.5	1.8
$\tau = \tau(\theta)$	τ [s]	156	71	48

b)

λ_T [W/mK]	c_T [mJ/gK]	ρ_0 [g/mm^3]	α_T [1/K]
0.27	1470000	71	$8.76 \cdot 10^{-5}$

3.2 Model validation

As a validation, to assess the capabilities of the constitutive model, a structural example with a multiaxial stress state is conducted. Therefore, experimental results of [17] for a Polyamide 6 sample (type 5A of ISO 527-2:2012) with a circular hole are compared to simulative results. The specimen with a degree of crystallinity of 23% is modified carefully with a circular hole of 1 mm diameter in the center of the gauge (see Fig. 3) and loaded under displacement controlled with a velocity of $v = 5$mm/min by a Zwick Z005 universal testing machine. During the test procedure, a heterogeneous strain field arose close to the hole, which is measured by a 2D ARAMIS 4M digital image correlation system with a chosen facet size of 14 x 14 pixel. Due to a homogeneous

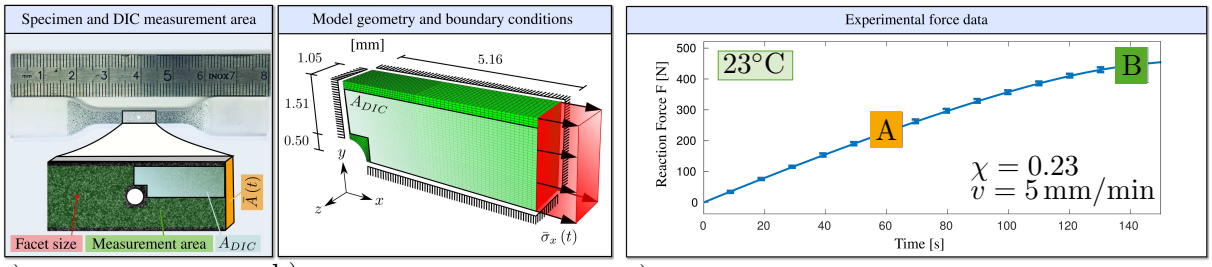

a) b) c)

Figure 3: Structural validation example: a) Geometry of the specimen with circular hole and DIC measurement area b) Finite element model including boundary conditions c) Recorded force data [17].

strain field visible at the outer boundary of the specimen, the evolution of the cross section $\bar{A}(t)$ can be deducted by means of the initial cross section A_0 and the mean stretch in transversal y-direction $\bar{\lambda}_y(t)$. In this way, the evolution of the true stress in x-direction at the boundary of the measuring field can be computed from the measured force data $F(t)$

$$\bar{\sigma}_x(t) = \frac{F(t)}{\bar{\lambda}_y(t)^2 A_0} \tag{26}$$

and used as a traction boundary for the FEM model (see Fig. 3). The comparison between experiment and simulation in terms of engineering strain contours is shown in Fig. 4 for two distinct time steps A($t = 60$ s) and B($t = 140$ s), highlighted in the force time relation (see Fig. 3). Due to the chosen facet size, no experimental data is available close to the imperfection, therefore this region is omitted in the comparison. A good agreement between experiment and simulation for horizontal and longitudinal direction is observed for both time steps. Considering the model identification procedure soley against monotonic tensile results, the good agreement of the multiaxial strain field close to the hole in experiment and simulation is particularly exceptional.

4 CONCLUSION

In this work, a framework for modeling semi-crystalline polymers at large strains under various temperatures and degrees of crystallinity is proposed to capture the material behavior of Polyamide 6. Inherent to the model is an additive decomposition into an elastoplastic as well as a viscoelastic contribution, both dependent on temperature as well as degree of crystallinity. The elastoplastic part is extended with an Arruda-Boyce type defect energy, to model kinematic hardening in a thermodynamic consistent way. In addition to the assumption of associative plasticity, a Tschoegel type yield surface is introduced, to account for a tension-compression asymmetry in yielding. After the implementation of the constitutive framework into the software ABAQUS, a model characterization with experimental results is carried out. Here, a staggered identification scheme for the isothermal model is used to identify the material constants for each temperature seperately, independent of strain rate and degree of crystallinity. A prediction of monotonic tensile tests at larger strain rate, serves as a first model validation. A good agreement between experiment and simulation is observed in the regime before material self-heating occured. Consequently, further validation examples are conducted, to assess the model

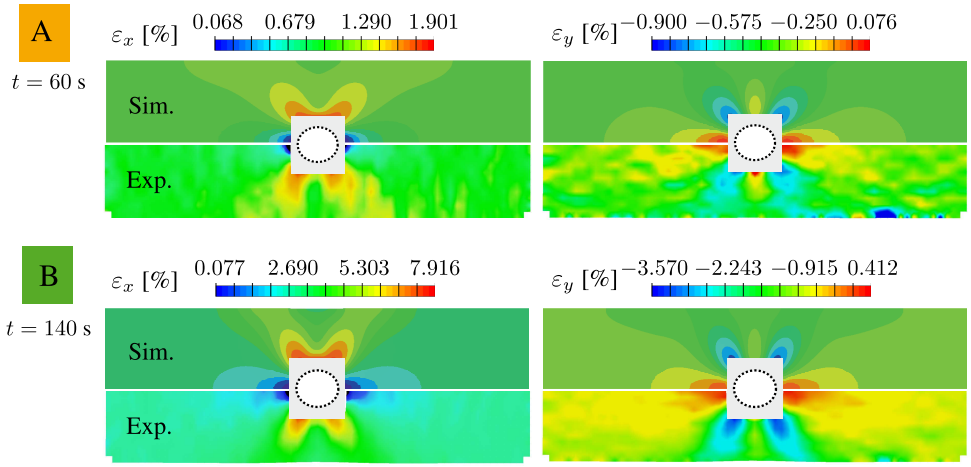

Figure 4: Engineering strain contour plots for two different time steps A and B - Comparison of Experimental data (Exp.) and corresponding model response (Sim.) in the A_{DIC} area (cf. Fig. 2). The strains in the grey area surrounding the hole are not provided, due to the chosen facet size (see [17]).

capability for multiaxial stress states. For that, experimental results of a tensile specimen with circular recess are taken from the literature and compared to simulative results. Also in this case, a good agreement with the experimental results is observed. The multiaxial stress state at the vicinity of the recess is well captured, indicating that the identification scheme against monotonic tensile tests alone is sufficient for the model characterization.
In the future, an extended experimental study over a wide range of degrees of crystallinity($20 - 40\%$) and temperatures will is planned to improve the characterization and model prediction even further. Therefore, the relaxation function will be fitted to experimental data and compression tests will yield insight on the yielding behavior under tension. Moreover, combined tension-compression tests will be carried out to better characterize the kinematic hardening.

ACKNOWLEDGEMENTS

Financial support by the German Science Foundation (DFG) (RE 1057/52-1, project number 454873500) is gratefully acknowledged. In addition, S. Reese acknowledges the funding of the projects RE 1057/46-1 (DFG, project number 404502442) and RE 1057/53-1 (SPP2311) (DFG, project number 465213526) and together with T. Brepols, the financial support for project TRR339 B05 (DFG, project number 453596084).

REFERENCES

[1] S. Felder, H. Holthusen, S. Hesseler, F. Pohlkemper, T. Gries, J.-W. Simon and S. Reese, Incorporating crystallinity distributions into a thermo-mechanically coupled constitutive model for semi-crystalline polymers, *Int. J. Plast.*, Vol. **135**, 102751, 2020.

[2] L. Anand, N. M. Ames, V. Srivastava and S. A. Chester, A thermo-mechanically coupled theory for large deformations of amorphous polymers. Part I: Formulation. *Int. J. Plast.*, Vol. **25**, pp. 1474–1494, 2009.

[3] I. Vladimirov, M. Pietryga and S. Reese, On the modelling of non-linear kinemtaic hardening at finite strains with application to springback - Comparison of time integration algorithms, *Int. J. Numer. Meth. Eng.*, Vol. **75**, pp. 1–28, 2008.

[4] T. Fornes, D. Paul, Crystallization behavior of nylon 6 nanocomposites, *Polym. J.*, Vol. **44 (14)**, pp. 3945–3961, 2003.

[5] R.N. Haward, G. Thackray, and T.M. Sugden, The use of a mathematical model to describe isothermal stress-strain curves in glassy thermoplastics, *Proc. R. Soc. Lond. Ser.A* , Vol. **302 (1471)**, pp. 453–472, 1968.

[6] M. Boyce, S. Socrate, and P. Llana, Constitutive model for the finite deformation stress-strain behavior of poly(ethylene terephthalate) above the glass transition, *Polym. J.* , Vol. **41 (6)**, pp. 2183–2201, 2000.

[7] V. Srivastava, S. A. Chester, N. M. Ames and L. Anand, A thermo-mechanically-coupled large-deformation theory for amorphous polymers in a temperature range which spans their glass transition, *Int. J. Plast.*, Vol. **26 (8)**, pp. 1138–1182, 2010.

[8] J.A.W. van Dommelen, D. M. Parks, M. C. Boyce, W.A.M. Brekelmanns and F.P.T. Baaijens, Micromechanical modeling of the elasto-viscoplastic behavior of semi-crystalline polymers, *J. Mech. Phys. Solids* , Vol. **51 (3)**, pp. 519–541, 2003.

[9] G. Ayoub, F. Zaïri, C. Fréderix, J. Gloaguen, M. Naït-Abdelaziz, R. Seguela and J. Lefebvre, Effects of crystal content on the mechanical behaviour of polyethylene under finite strains: experiments and constitutive modelling, *Int. J. Plast.*, Vol. **24 (4)**, pp.492–511, 2011.

[10] T. Barriere, X. Gabrion and S. Holopainen, A compact constitutive model to describe the viscoelastic-plastic behaviour of glassy polymers: comparison with monotonic and cyclic experiments and state-of-the-art models, *Int. J. Plast.*, Vol. **122**, pp. 31–48, 2019.

[11] B. Miled, I. Doghri and L. Delannay, Coupled viscoelastic-viscoplastic modeling of homogeneous and isotropic polymers: numerical algorithm and analytical solutions, *Comput. Methods Appl. Mech. Eng.* , Vol. **200 (47)**, pp. 3381–3394, 2011.

[12] M.R. Gudimetla and I. Doghri, A finite strain thermodynamically-based constitutive framework coupling viscoelasticity and viscoplasticity with application to glassy polymers, *Int. J. Plast.*, Vol. **98**, pp. 197–216, 2017.

[13] F. Praud, G. Chatzigeorgiou, J. Bikard and F. Meraghni, Phenomenological multimechanisms constitutive modelling for thermoplastic polymers, implicit implementation and experimental validation, *Mech. Mater.*, Vol. **114**, pp. 9–29, 2017.

[14] J. Wang, L.F. Peng, Y.J. Deng, X.M. Lai, M.W. Fu and J. Ni, A finite strain thermodynamically-based constitutive modeling and analysis of viscoelastic-viscoplastic deformation behavior of glassy polymers, *Int. J. Plast.*, 2019.

[15] W. Li, G. Gazonas, E.N. Brown, P.J. Rae and M. Negahban, Thermomechanical model for monotonic and cyclic loading of peek, *Mech. Mater.*, Vol. **129**, pp. 113–138, 2019.

[16] F. Shen, G. Kang, Y.C. Lam, Y. Liu and K. Zhou, Thermo-elastic-viscoplastic-damage model for self-heating and mechanical behavior of thermoplastic polymers, *Int. J. Plast.*, Vol. **121**, pp. 227–243, 2019.

[17] S. Felder, N. A. Vu, S. Reese and J.-W. Simon, Modeling the effect of temperature and degree of crystallinity on the mechanical response of Polyamide 6, *Mech. Mater.*, Vol. **148**, pp. 103476, 2020.

[18] E. Ghorbel, A viscoplastic constitutive model for polymeric materials, *Int. J. Plast.*, Vol. **24(11)**, pp. 2032–2058, 2008.

[19] A. R. Melro, P. P. Camanho, F. A. Pires and S. T. Pinho, Micromechanical analysis of polymer composites reinforced by unidirectional fibres: Part I - Constitutive modelling, *Int. J. Solid. Struct*, Vol. **50**, pp. 1897–1905, 2013.

[20] C. Eckart, The thermodynamics of irreversible processes. IV. The theory of elasticity and anelasticity, *Phys. Rev.*, Vol. **73 (4)**, pp. 373–382, 1948.

[21] E. Kröner, Allgemeine Kontinuumstheorie der Versetzungen und Eigenspannungen, *Arch. Ration. Mech. Anal.*, Vol. **4 (1)**, pp. 273–334, 1959.

[22] E. H. Lee, Elastic-plastic deformation at finite strains, *J. Appl. Mech*, Vol. **36 (1)**, pp. 1–6, 1969.

[23] F. Sidoroff, Un modele viscoelastique non lineaire avec configuration intermediaire, *J. Mech.*, Vol. **13**, pp. 679–713, 1974.

[24] J. Lubliner, A model of rubber viscoelasticity, *Mech. Res. Commun*, Vol. **12 (2)**, pp. 93–99, 1985.

[25] S. Reese and S. Govindjee, Theoretical and numerical aspects in the thermo-viscoelastic material behaviour of rubber-like polymers, *Mech. Time-Dependent Mater.*, Vol. **1 (4)**, pp. 357–396, 1998.

[26] T. Brepols, S. Wulfinghoff and S. Reese, A gradient-extended two-surface-plasticity model for large deformations, *Int. J. Plast.*, Vol. **129**, 102635, 2020.

[27] A. Khan and B. Farrokh, Thermo-mechanical response of nylon 101 under uniaxial and multi-axial loadings: Part I. Experimental results over wide ranges of temperatures and strain rates, *Int. J. Plast.*, Vol. **22**, pp. 1506–1529, 2006.

[28] N. W. Tschoegel, Failure surfaces in principal stress space, *J. Polym. Sci.*, Vol. **32**, pp. 239–267, 1971.

[29] E.M. Arruda and M. C. Boyce, A three-dimensional constitutive model for the large stretch behavior of rubber elastic materials, *J. Mech. Phys. Solid.*, Vol. **41 (2)**, pp. 389–412, 1993.

[30] M. Kaliske and H. Rothert, On the finite element implementation of rubber-like materials at finite strains, *Eng. Comput.*, Vol. **14 (2)**, pp. 216–232, 1997.